Contributions to Mineralogy and Petrology (2021) 176:80
https://doi.org/10.1007/s00410-021-01841-1

ORIGINAL PAPER

Fast grain-boundary ionic conduction in multiphase aggregates as revealed by electrical conductivity measurements

Kui Han[1,2] · Xinzhuan Guo[3,4] · Junfeng Zhang[4] · Xuben Wang[1] · Simon M. Clark[2]

Received: 7 June 2021 / Accepted: 11 September 2021 / Published online: 23 September 2021

Abstract

Interpretation of deep earth structures from electromagnetic data requires the constraint from the electrical conductivity of various minerals experimentally measured at high temperature and high pressure. However, the combination of these measured conductivities of different minerals always fails to match the conductivities of the multiphase rocks under in-situ conditions. To investigate the effect of ion segregation at grain boundaries on bulk conductivity, we measured the electrical conductivities of quartz, albite, and orthoclase single-phase aggregates, as well as those of two multiphase aggregates made up of the three minerals at both ambient pressure and 1 GPa over a range of temperatures. The electrical conductivities of the multiphase aggregates were an order of magnitude higher and the activation enthalpies were lower than those of the three single-phase aggregates. A significant dependence of conductivity on grain size was identified in the multiphase aggregates but not in the single-phase aggregates. The interdiffusion of alkali ions between orthoclase and albite initiated grain boundary ionic conduction, which enhanced the bulk conductivity of the multiphase aggregates to 20 S/m at 1073 K. This conduction mechanism might explain the electrical conductivity anomalies of the active shear zone in the crust.

Keywords Electrical conductivity · Grain-boundary · Ionic conduction · High conductivity anomalies

Introduction

Electrical conductivity as deciphered by magnetotellurics (MT) and electromagnetics is useful for understanding the composition and architecture of the deep earth (Robertson et al. 2016; Amulele et al. 2019; Özaydın and Selway 2020). The chemical composition of minerals, such as hydrogen and iron content, can strongly affect their conductivities (Li et al. 2017; Karato 2019; Dai and Karato 2020; Fei et al. 2020). When various minerals are assembled as rocks, the bulk conductivities of those rocks are determined not only by their constituent minerals and relative proportions, but also by various physiochemical processes (Jones et al. 2012; Karato and Wang 2013; Guo et al. 2015). Therefore, a knowledge of how constituent minerals control the bulk conductivity of rocks is critical for extracting information about in situ rocks from geophysical observations, such as water content and fraction of melts, given the inaccessibility of rocks and their compositional variation in the deep earth (Khan and Shankland 2012; Laumonier et al. 2017; Guo et al. 2018).

The conductivities of rock-forming minerals derived from laboratory conduction models are usually combined to calculate the bulk conductivity of a rock using mixing models. However, the combined conductivities of minerals have always been found to be inconsistent with that of a whole rock determined by geophysical observation. For example, Jones et al. (2012) combined the electrical conductivities of olivine, pyroxene, and garnet to model the conductivity of the kimberlite beneath the Southern Africa Craton. However, their calculation based on the data of Karato and

Communicated by Hans Keppler.

✉ Xinzhuan Guo
gxzhuan@mail.gyig.ac.cn

1 College of Geophysics, Chengdu University of Technology, Chengdu 610059, Sichuan, China

2 ARC Centre of Excellence for Core To Crust Fluid Systems and Department of Earth and Environmental Sciences, Macquarie University, Sydney, NSW 2109, Australia

3 Key Laboratory of High-Temperature and High-Pressure Study of the Earth's Interior, Institute of Geochemistry, Chinese Academy of Sciences, Guiyang 550000, Guizhou, China

4 State Key Laboratory of Geological Processes and Mineral Resources, China University of Geosciences, Wuhan 430074, Hubei, China

Wang (2013) is higher than the conductivity data from the MT observation, while the calculated values based on the data of Poe et al. (2010) and Yoshino et al. (2009) were lower than the observed values (Fig. 1). Wang et al. (2014b) also modelled the conductivity of a lherzolite by combining the conductivities of its constitutive minerals, whereas the calculation could not match the conductivity observed by MT despite the analogy of their modal composition. This discrepancy could be related to either the compositional difference between the constituent minerals and the rock or to the inappropriate mixing models due to the complexity of the geometry. Another possibility is that fast grain-boundary diffusivity of ions was not considered in the model computing. Given the requirement for chemical equilibrium in the multiphase aggregates, the partitioning of charge carriers, such as protons between different minerals, has been considered before laboratory models were used to calculate the conductivities of minerals and combined to give the bulk conductivity (Aubaud et al. 2004; Grant et al. 2007; Jones et al. 2012; Wang et al. 2014b; Han and Clark 2021). However, when segregated from the minerals, these charge carriers might reside at grain boundaries, forming a reservoir (Hiraga et al. 2004; Dohmen 2008). Since grain-boundary

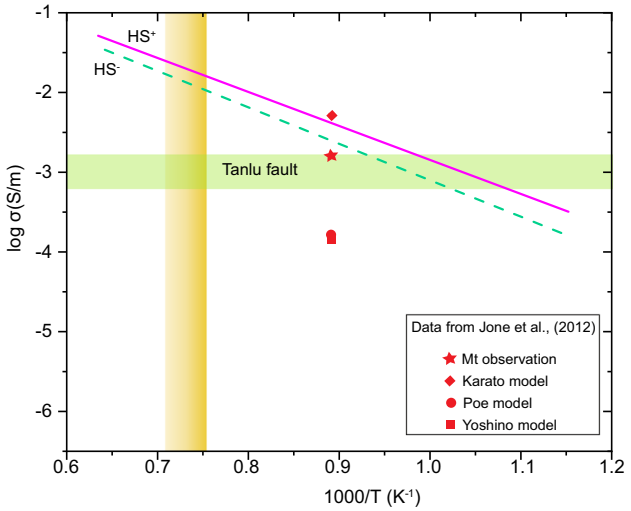

Fig. 1 Representative discrepancies between MT observation and laboratory calculations. The red star denotes the observed electrical conductivity of Jagersfontein peridotite at 750 °C from South Africa, while the red diamond, circle, and square are the calculated conductivities based on the proton conduction model of Karato, Peo and Yoshino, respectively (Karato and Wang 2013; Poe et al. 2010; Yoshino et al. 2009). The solid blue line is the measured electrical conductivity of a lherzolite mantle xenolith, from Nushan in the North China Craton, near the Tanlu Fault (Wang et al. 2014b). The light green shadow is the electrical conductivity observed by MT under the Tanlu Fault. The solid pink and dashed green lines are the Hashin–Shtrikman (HS) upper and lower bound, respectively, of calculated electrical conductivity, using the composition similar to the lherzolite mantle xenolith without water

diffusivity can be several orders of magnitude higher than volume diffusivity (Farver et al. 1994; Dohmen and Milke 2010), the fast transport of these charge carriers at grain boundaries might induce grain-boundary conduction and enhance the bulk conductivity (Ten Grotenhuis et al. 2004). In this case, highly conductive phases, such as melts (Ni et al. 2011; Guo et al. 2018), aqueous fluids (Guo et al. 2015), and graphite (Yoshino and Noritake 2011) are no longer necessary. Unfortunately, previous studies have focused mainly on either single-phase aggregates with varying grain sizes or aggregates bearing a conductive phase, such as melts, sulphite, and graphite films (Roberts and Tyburczy 1991; Ducea and Park 2000; Ten Grotenhuis et al. 2004; Watson et al. 2010; Yang and Heidelbach 2012). For multiphase aggregates, Jones (2016) estimated the contribution of grain-boundary conduction due to proton segregation to model the bulk conductivity of peridotite aggregates, but this has not been confirmed by laboratory conductivity measurements, and Jones neglected other potential charge carriers at the grain boundaries. Until now, to our knowledge, no experiments have been conducted on multiphase aggregates to verify this hypothesis.

To test this hypothesis, we investigated the electrical conductivity of single-phase aggregates of quartz, albite, and orthoclase and multiphase aggregates containing quartz, albite, and orthoclase with different grain sizes at both ambient pressure and 1 GPa and at various temperatures below the solidus. We identified significant grain-boundary conduction, which resulted in discrepancies between the measured and calculated bulk conductivities based on different geometry models. We further applied the experimental results to explain the high conductivity anomalies in the crust within active geological settings.

Experimental methods

Sample characterization and preparation

Three natural samples of quartzite, albite, and perthite were chosen from the hand-collected specimens (storage number: MU 637, MU 13,072 and MU13068) of the Department of Earth and Environmental Sciences (DEES), Macquarie University, Australia, to prepare the starting materials. Quartzite (Qtz-R) is transparent and consists of nearly pure quartz, with fluid inclusions visible under the microscope. Perthite (Or-R) is composed of orthoclase as the host mineral and albite as exsolution lamellae. Albite (Ab-R) shows a structure of core and mantle sub-grains under the microscope, suggesting a history of slight deformation.

The chemical compositions of Qtz-R and Ab-R were determined using a Cameca SX-100 electron microprobe in the Macquarie University GeoAnalytical unit (MQGA)

in the DEES, using an accelerating voltage of 15 kV and a current of 20 nA. The beam size was set at 10 μm. X-ray fluorescence (XRF) was used to determine the bulk composition of the perthitic Or-R. The details of the chemical compositions are listed in Table 1.

Qtz-R, Ab-R, and Or-R were ground using ethanol and acetone in an agate mortar. The samples with grain sizes of approximately 20 μm were labelled Ab-P, Qtz-P, and Or-P, and those with grain sizes of 100–300 μm were labelled Ab-G, Qtz-G, and Or-G. A mixture of 41.7 wt% quartz, 21.6 wt% albite, and 36.7 wt% orthoclase was used to generate two multiphase aggregates with grain sizes of 20 μm and 100–300 μm, labelled MA1-P and MA1-G, respectively. Another mixture of 37.7 wt% quartz, 44.5 wt% albite and 16.9 wt% orthoclase was used to generate two multiphase aggregates of MA2-P and MA2-G with the different grain sizes given above.

For measurements at ambient pressure, Qtz-P, Ab-P, and Or-P were blended using 5% vinyl alcohol (CH_2CHOH) solution as a chemical adhesive, which acted as a binder, allowing for better compaction. These blended aggregates were then manually pressed into pellets and annealed at 1173 K for approximately 4 h in an oven. The MA1-P and MA2-P aggregates were also mixed using 5% vinyl alcohol (CH_2CHOH) and compressed in the same manner. The aggregates were then annealed at 823 K, well below the melting point of granite, for 4 h to decompose the vinyl alcohol and were then kept at 1173 K for an additional 4 h. The vinyl alcohol solution was completely removed at 503 K. No silicate melts were observed in any of the pellets following annealing.

For measurements at 1 GPa, the powder samples (Ab-P, Qtz-P, Or-P, MA1-P, and MA2-P) were pressed into pellets and inserted into MgO sample sleeves. The Ab-G, Qtz-G, MA1-G, and MA2-G pellets were first compacted manually, and then sealed in nickel capsules. The Ab-G and Qtz-G pellets were then hot-pressed at approximately1 GPa and 1073 K using a piston-cylinder apparatus in the DEES, while the MA1-G and MA2-G pellets were hot-pressed at approximately1 GPa and 773 K. The apparatus used is described by Adam and Green (1994). A 10% correction was applied to the measured pressures to allow for the effect of friction, which gave an error of ± 0.1% for the true pressures. Temperatures were measured using a $Pt–Pt_{90}Rh_{10}$ thermocouple with an accuracy of ± 10 K. These hot-pressed samples were drilled into discs of 2 mm diameter and polished to a thickness of 1 mm. The discs were cleaned using distilled water, ethanol, and acetone and then stored in a vacuum oven before sample assembly. The Or-G disc was prepared as a 2 mm diameter × 1 mm disc without hot pressing. These samples were stored in an oven at 393 K for more than 24 h.

Electrical conductivity measurements

The electrical conductivity measurements at 1 GPa were performed on a Walker-type Rockland 1000-ton apparatus at the State Key Laboratory of Geological Processes and Mineral Resources (SKL-GPMR), China University of Geosciences (CUG), Wuhan, China. All of the powder and grain aggregates prepared for the measurements at 1 GPa were packed into MgO sleeves, which were then capped with two nickel electrodes. 25/15 octahedral cells

Table 1 Chemical compositions of Qtz-R, Ab-R, and Or-R specimens, and of the constituents of MA1-G after the conductivity measurement in this study

Oxide	Starting material			MA1-G		
	Qtz-R	Ab-R	Or-R	Quartz[1]	Albite[1]	Orthoclase[1]
SiO_2	99.45	69.84	65.49	99.78	67.18	64.18
TiO_2	0	0	0	0	0	0
Al_2O_3	0	19.82	19.36	0	21.06	18.98
FeO	0	0.03	0.02	0	0	0
MnO	0	0	0	0	0	0
MgO	0	0	0.07	0.01	0	0.01
CaO	0	0.35	0.05	0.01	0.8	0
Na_2O	0	11.36	3.71	0	11.39	1.72
K_2O	0.01	0.07	11.73	0.01	0.08	14.51
NiO	0.01	0	0	0.02	0	0
P_2O_5	0	0	0.36	0	0	0
Total	99.47	101.45	100.79	99.83	100.52	99.4
MA1	41.70%	21.60%	36.70%			
MA2	37.70%	44.50%	16.90%			

[1]The chemical compositions of the minerals were probed from the core areas of the grains in MA1-G after the conductivity measurements

[2]The weight percentages of the constituent minerals in MA1 and MA2 are given at the bottom of the table

(octahedral edge length/truncation edge length in mm) were used to accommodate the sample assemblies. The detailed configuration of the assembly and the calibration of the press follow the description by Li et al. (2018). The completed assemblies were stored in a dry vacuum oven before being loaded into the apparatus. The electrical conductivity was determined by impedance spectroscopy measurements collected from an AMETEK® Solartron 1296 impedance gain-phase analyzer under alternating current. The voltage of the bridge was set to 0.707 V and the applied frequency ranged from 0.1 to 10^6 Hz. The temperature was raised only after the pressure had stabilized at 1 GPa. Electrical conductivity measurements were carried out until the observed resistance remained relatively constant at each temperature, which suggested that the samples had reached equilibrium.

Given that quartz and feldspar could begin to melt at a low temperature (e.g., 923 K) in the presence of water, the MA1-G and MA2-G pellets were heated and kept at 873 K for more than 1 h to expel any absorbed water in the assemblies. In addition, the MA1-P was heated to 873 K and held at that temperature for 1 h to expel any absorbed water in the assembly, as well as thoroughly press the samples. The MA2-P pellet was heated to 773 K, followed by 5 h of annealing at 773 K. The temperature was increased to 1273 K and then decreased once the readings had stabilized. The impedance data of all samples were measured during more than two heating cooling cycles. In particular, MA1-G were measured at both low (< 873 K) and high (> 873 K) temperature for several circles.

The measurements at ambient pressure were performed in an argon atmosphere, using an MTZ-35 impedance analyzer, in the School of Chemistry, University of Sydney, Sydney, Australia. The two electrodes were made of copper. The applied voltage was 0.5 V, and the frequency varied from 0.1 to 10^7 Hz. The temperature for these measurements was steadily and continuously increased from room temperature to 1173 K at a rate of 20 K per minute. At least one cycle of heating and cooling was performed during each measurement run. For ambient and 1 GPa conditions, the resulting impedance spectra were simulated using an equivalent circuit consisting of a resistor and a constant phase element in parallel to obtain the resistance of the sample. The electrical conductivity was then calculated from the equation:

$$\sigma = l/SR \tag{1}$$

where S is the surface area of the sample pellets, l is the sample thickness and R is the resistance. The dimensions used in this calculation were determined by averaging the sample dimensions before and after the conductivity measurements, yielding an error of less than 10%.

Fourier transform infrared measurements

The water content of the samples was determined using Fourier transform infrared (FTIR) spectroscopy before and after the electrical conductivity measurements. FTIR has been widely used to determine the water content in several polycrystalline systems, such as pyroxene, plagioclase, and olivine (Yang et al. 2012). Our sample sections were polished on both sides without distinguishing the crystallographic orientations. These samples were heated to 473 K in a vacuum oven for at least 8 h prior to FTIR analysis to remove any water absorbed on the surface. Unpolarized light was used for the powder samples containing random grain orientations, allowing for acceptable estimates of water content with uncertainty of less than 20%, even though the absorbance has been found to change with orientations for anisotropic minerals (Rossman 2006). The FTIR spectra were collected using a Nicolet 6700 instrument, at the SKL-GPMR, CUG. The apparatus was equipped with mercury cadmium telluride (MCT) detector, tungsten light source, and KBr beam splitter. The aperture was 100 μm giving a spot size of 100 × 100 μm. A total of 128 scans were acquired at 4 cm^{-1} resolution. The background absorption (the absorption or the air) was subtracted during the measurements. The spectra at the range of 3000–4000 cm^{-1}, characteristic for hydrogen-related species, were processed by baseline correction using the spline fitting method (Aines and Rossman 1984; Rossman 2006). The water concentration was determined using the modified Beer–Lambert law, $A = Ict\gamma$, where A is the total integral absorbance (cm^{-1}), I is the integral molar absorption coefficient, c is the concentration, t is the thickness of the samples, and γ is the orientation factor. The orientation factor for single crystals prior to the conductivity measurements was 1/3, while for the polycrystalline samples following the measurements was 1 because of the random orientation (Rossman 2006). An integral molar absorption coefficient of 13.0 ± 2.2 $ppmw^{-1}$ cm^{-2} was adopted for the quartz samples (Thomas et al. 2009). Integral absorption coefficients of 17.1 ± 1.6 $ppmw^{-1}$ cm^{-2} and 29.3 ± 3.0 $ppmw^{-1}$ cm^{-2} were used for the orthoclase and albite samples, respectively (Mosenfelder et al. 2015). The integral molar absorption coefficients for MA1-P and MA2-P were calculated from the relative volume percentage of each constituent phase, resulting in values of 18.0 $ppmw^{-1}$ cm^{-2} for MA1-P, and 21.1 $ppmw^{-1}$ cm^{-2} for MA2-P. The likely error was ± 10% based on the accuracy of the absorption coefficients.

Following the impedance spectroscopy measurements, the recovered samples were imaged using a Quanta FEI 450 scanning electronic microscope installed at the SKL-GPMR, CUG. Line analysis of the chemical compositions was conducted across the orthoclase and albite grains in MA1-G

using the Cameca® SX-100 electron microprobe at the MQGA. Beam size was set at 1 μm for the line analysis to attain a better resolution for the variations in concentration.

Results

Figure 2 shows the representative infrared spectra of the samples taken before and after the electrical conductivity measurements. In Fig. 2a, Ab-G and Ab-P after the measurements show a major band at 3500 cm^{-1}, indicating the presence of type I OH, which is found in natural metamorphic and pegmatitic albites (Johnson and Rossman 2004; Rossman 2006). The absorbance increased considerably after the measurements of Ab-G and Ab-P. Or-R displayed a sharp peak at 3623 cm^{-1}, implying the presence of type I H_2O, which disappeared in the spectra of Or-P and Or-G after the conductivity measurements (Johnson and Rossman 2004). Or-G after the measurements displayed a major band at 3427 cm^{-1}, which was likely the shifted band at 3369 cm^{-1} in Or-R. The absorbance of Or-G was similar to that of Or-R but appreciably lower than that of Or-P. Qtz-G and the Qtz-P showed a similar absorbance at 3460 cm^{-1}, which might have shifted from the 3388 cm^{-1} band of Qtz-R. The H-related intensities of Qtz-G and Qtz-P were about twice that of Qtz-R. MA1-P displayed an appreciable peak at 3620 cm^{-1} that was consistent with that found in Or-R. We use the term "water" to include most of hydrogen species, including molecular H_2O and hydroxyl, found within the range 3000–3800 cm^{-1}. The calculated water content of all of the samples are listed in Table 2. Ab-R was almost "dry" (10.84 ppm H_2O), but the water content increased by 30 times in Ab-G (368 ± 77 ppm H_2O) and 50 times in Ab-P (492.69 ± 49 ppm H_2O). The water content of Or-G rarely changed from its starting value, but increased by almost a factor of three in Or-P. Qtz-G and Qtz-P contained similar water contents, nearly 50% higher than that of Qtz-R. MA1-P contained 209 ± 20 ppm H_2O, much lower than those of Ab-P, Or-P, and Qtz-P. The increase of water content after conductivity measurements indicates that a small amount of

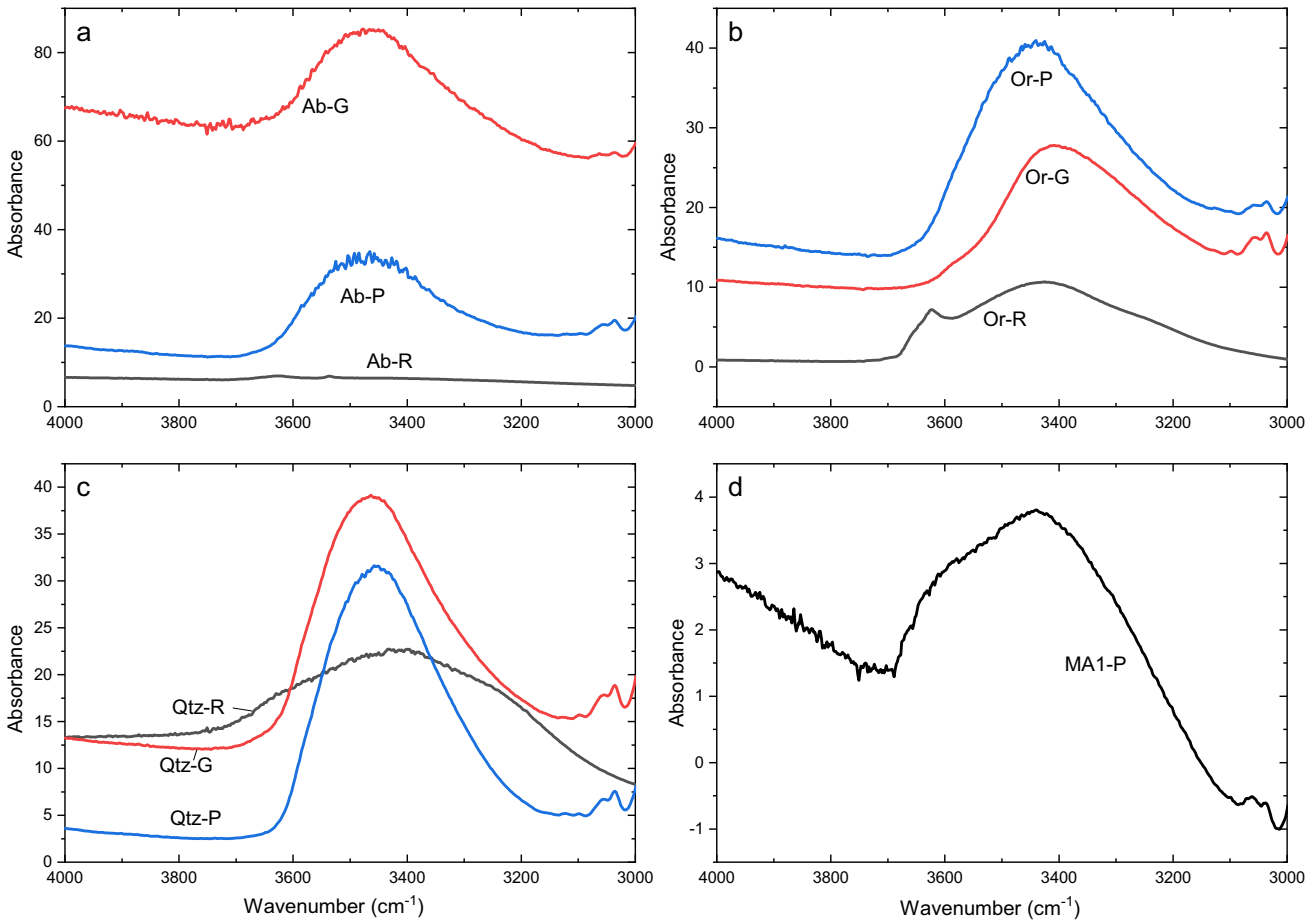

Fig. 2 Representative infrared spectra of samples before and after the conductivity measurements. The spectra before the conductivity measurements were obtained from the starting materials, Ab-R, Or-R, and Qtz-R, which are presented by the black dotted lines. The red solid and blue dash–dotted lines denote the IR spectra of different samples obtained after the conductivity measurements

Table 2 Temperature and pressure conditions for the electrical conductivity measurements, water content of initial samples before and after the conductivity measurements, and Arrhenius parameters of the samples

Sample	T (K)	P (GPa)	Water content (ppm H_2O)		ΔH (eV)	A (S/m)
			Initial	Final		
Qtz-P	873–1273	1	940 (±285)	1489 (±256)	0.968 (±0.028)	4.2
Qtz-P	473–1173	Ambient			0.896 (±0.018)	1.2
Qtz-G	873–1273	1	940 (±285)	1359 (±156)	1.18 (±0.11)	4.7
Ab-P	673–1273	1	11 (±5)	493 (±49)	0.951 (±0.057)	5.9
Ab-P	473–1173	Ambient	–	–	0.907 (±0.023)	1.1
Ab-G	873–1273	1	11 (5)	368 (±77)	0.880 (±0.031)	1.2
Or-P	673–1273	1	468 (±133)	1224 (±115)	0.951 (±0.045)	5.4
Or-P	473–1173	Ambient			0.814 (±0.013)	2.1
Or-G	873–1273	1	468 (±133)	578 (±114)	1.32 (±0.041)	235.3
MA1-P	673–1273	1	–	209 (±21)	0.776 (±0.012)	7.1
MA1-P	473–1173	Ambient	–	–	0.781 (±0.013)	1.1
MA1-G	673–1273	1	–	–	0.771 (±0.021)	3.1
MA2-P	673–1273	1	–	–	0.799 (±0.089)	14.4
MA2-P	473–1173	Ambient	–	–	0.775 (±0.086)	2.4
MA2-G	673–1273	1	–	–	0.871 (±0.070)	4.0

The initial water contents of Qtz-P, Ab-P, and Or-P were derived from the FTIR measurements of their corresponding starting materials, Qtz-R, Ab-R, and Or-R, respectively. The values in parentheses are the standard deviation

water has been incorporated into both the single-phase and multiphase aggregates.

The complex impedance spectra of Qtz-P at 1 GPa and ambient pressure are shown in Fig. 3. The diagram is composed of the real and imaginary impedance. The impedance plots consist of one depressed arc, representing the electrical conductivities of the bulk aggregates, and a linear tail at low frequencies, indicating the electrode effects between the electrodes and the sample surfaces (Watson et al. 2010). The relationship between electrical conductivity and temperature is given by the Arrhenius equation in the form of logarithmic electrical conductivities as a function of reciprocal temperature. Several samples showed electrical conductivities at their first heating stage, which were inconsistent with the subsequent stages, probably due to the effect of absorbed water within the sample assemblies. Figure 4 shows only the stable values after the first heating stage. Qtz-G was measured only at the first heating stage because of thermocouple failure at the cooling stage. The electrical conductivity of Qtz-G at 1 GPa, showed good agreement with the conductivity of Qtz-P at both 1 GPa and ambient pressure, indicating the predominant role of lattice conduction from the grain interior and the slight effect of pressure on the conductivity of the quartz aggregates. The logarithmic conductivities for Or-G and Or-P at 1 GPa did not change linearly with the reciprocal temperature below 873 K, which could be attributed to either impurities or twin boundaries in the orthoclase grains (Nover 2005). Or-G showed consistent electrical conductivity with Or-P at 1 GPa, but higher conductivity than Or-P at ambient pressure. The segments of Or-P and Or-G above 923 K were used to fit the data to the Arrhenius equation. Ab-P measured at 1 GPa had half an order of magnitude higher conductivity than Ab-P at ambient pressure. MA1-P at 1 GPa showed about half an order of magnitude higher conductivity than MA1-G and about one order of magnitude higher than MA1-P at ambient pressure. The conductivity of MA2-P at 1 GPa was about one order of magnitude higher than that of MA2-G, which showed similar conductivity to MA2-P at ambient pressure. To calculate the activation energy, the electrical conductivities of all of the samples were expressed in the form of the Arrhenius equation:

$$\sigma = A \exp(-\Delta H / kT) \tag{2}$$

where A is a pre-exponential factor, T is the absolute temperature in kelvin, ΔH is the activation enthalpy, and k is the Boltzmann constant. The resulting activation enthalpy and pre-exponential factor for all of the samples are listed in Table 2.

For the single-phase aggregates, the activation enthalpies at 1 GPa were higher than those at ambient pressure. For example, the activation enthalpy of Ab-P was calculated to be 0.951 eV at 1 GPa, slightly higher than that of 0.907 eV at ambient pressure. The activation enthalpy of Or-P (0.951 eV) at 1 GPa was higher than that at ambient pressure (0.814 eV). Or-G and Qtz-G showed higher activation enthalpies than Or-P and Qtz-P, respectively. Overall, even though the activation energies of all of the single-phase aggregates were slightly different, most of them were in the range of 0.9–1 eV. By contrast, the multiphase

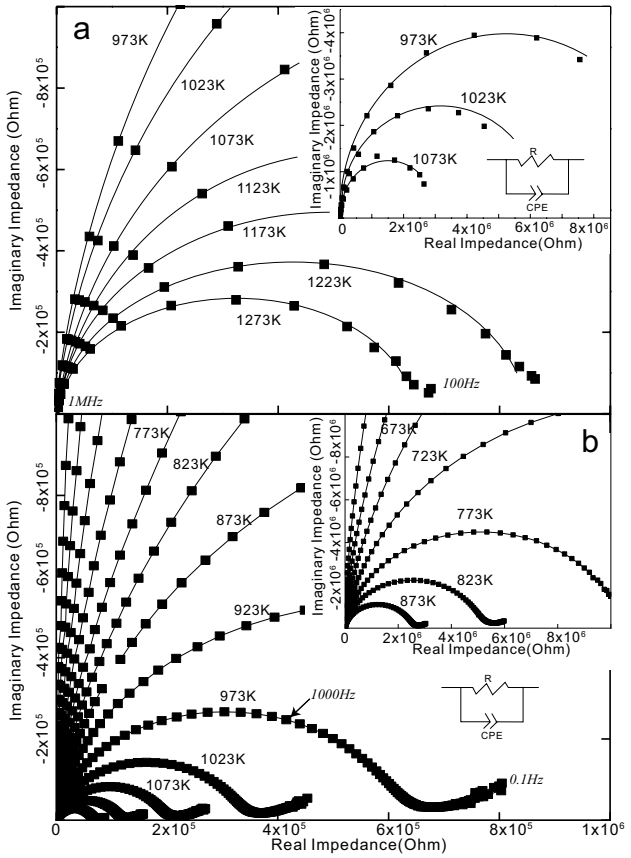

Fig. 3 Representative complex plane plots of Qtz-P at: **a** 1 GPa and **b** ambient pressure. The data points were acquired from high to low frequencies (from left to right). The electrical responses at low frequencies ended up with disarrayed patterns due to electrode polarization and surrounding disturbances. These points were excluded from the resistance calculation to allow for accurate interpretations. The impedance arcs were fitted using an equivalent circuit that comprised a constant phase element (CPE) and a single resistor (R) in parallel

aggregates showed similar activation enthalpies below 0.8 eV (except for MA2-G), remarkably lower than those of the single-phase aggregates at the corresponding pressures. For example, the activation enthalpies of MA1-P (0.78 eV) and MA1-P (0.80 eV) at 1 GPa were lower than those of Qtz-P, Ab-P, and Or-P at 1 GPa.

The equilibrium melting diagram shows that the dry solidus temperature for a quartz-albite-orthoclase aggregate is about 1373 K at 1 GPa (Fig. 5). Given that the effect of dissolved water (hundreds of ppm) in the multi-phase sample on reducing the solidus (Johannes and Holtz 2012), it is critical to examine the existence of melts in the multiphase aggregates. No melts were found at the triple junction of quartz-albite-orthoclase and other domains at 1 GPa by checking the back-scattered images of all the multiphase aggregates (Fig. 6b, and Figs. S2 and S3 in supplementary material). In addition, the conductivities of MA1-P and MA2-P show no abrupt increases at 1273 K (Fig. S4). If fractional melts were present and interconnected at high temperatures, the conductivity should increase by 1–2 orders of magnitude (Laumonier et al. 2017). Therefore, we suggest that the water in the multiphase aggregates at 1 GPa, about 209 ppm in MA1-P (Table 2), hardly reduced the solidus below 1273 K. At ambient pressure, the solidus temperature for a quartz-feldspar aggregate is about 1233 K (Tuttle and Bowen 1958). According to the relationship between the composition and minimum solidus temperature of a quartz-feldspar system, MA1-P and MA2-P both showed a melting point higher than 1233 K at ambient pressure (Fig. 5, insert). The annealing treatments and conductivity measurements on MA1-P and MA2-P were carried out below 1173 K at ambient pressure; thus, melting could hardly occur at ambient pressure. However, we could not exclude the possibility of the existence of small melt fractions undetectable in BSE images or by electrical conductivity measurements.

The back-scattering images reveal the occurrence of microcracks in Ab-G and MA1-P (Fig. 6a, b). These microcracks in Ab-G may have formed during either the hot-press treatment or the decompression following the measurements, while those in MA1-P were probably generated during the decompression, as fast and non-hydrostatic decompression generally gives rise to the propagation of microcracks. The morphology of the grains and the absence of structures associated with recrystallization indicate that the minerals had not yet been recrystallized. Note that cavities with arbitrary shapes (< 1 μm) were observed in some of the grains. In the powder multiphase aggregates, the Na^+ and K^+ ions are distributed throughout the grains and at the grain boundaries, leading to a change in chemical composition for the small feldspar grains (Fig. 6c, d), which means that Na^+ in albite had diffused into the orthoclase grains and, simultaneously, K^+ in orthoclase had diffused into the albite grains.

In MA1-G, the electron microprobe shows that the compositions of the constituent minerals differed from the core to the rim. To be specific, compared to the rim, the composition of the grain cores changed less from the initial values before the conductivity measurements (Table 1). The composition of the constitutive quartz in MA1-G changed little during the conductivity measurements. The concentration of Ca^{2+} ions in the albite grains increased slightly, but within experimental error. Within the orthoclase grains in MA1-G, the concentration of Na^+ decreased and that of K^+ increased in the radial direction of albite lamellae (Fig. S1 in supplementary material), suggesting that Na^+ in the albite lamellae had diffused into the orthoclase host, and K^+ had diffused into the albite lamellae. However, the inter-diffused distance was shown to be less than 10 μm, smaller than the orthoclase grain size, which indicates that the chemical composition of orthoclase was barely affected by albite lamellae. To investigate the chemical variations between the albite and

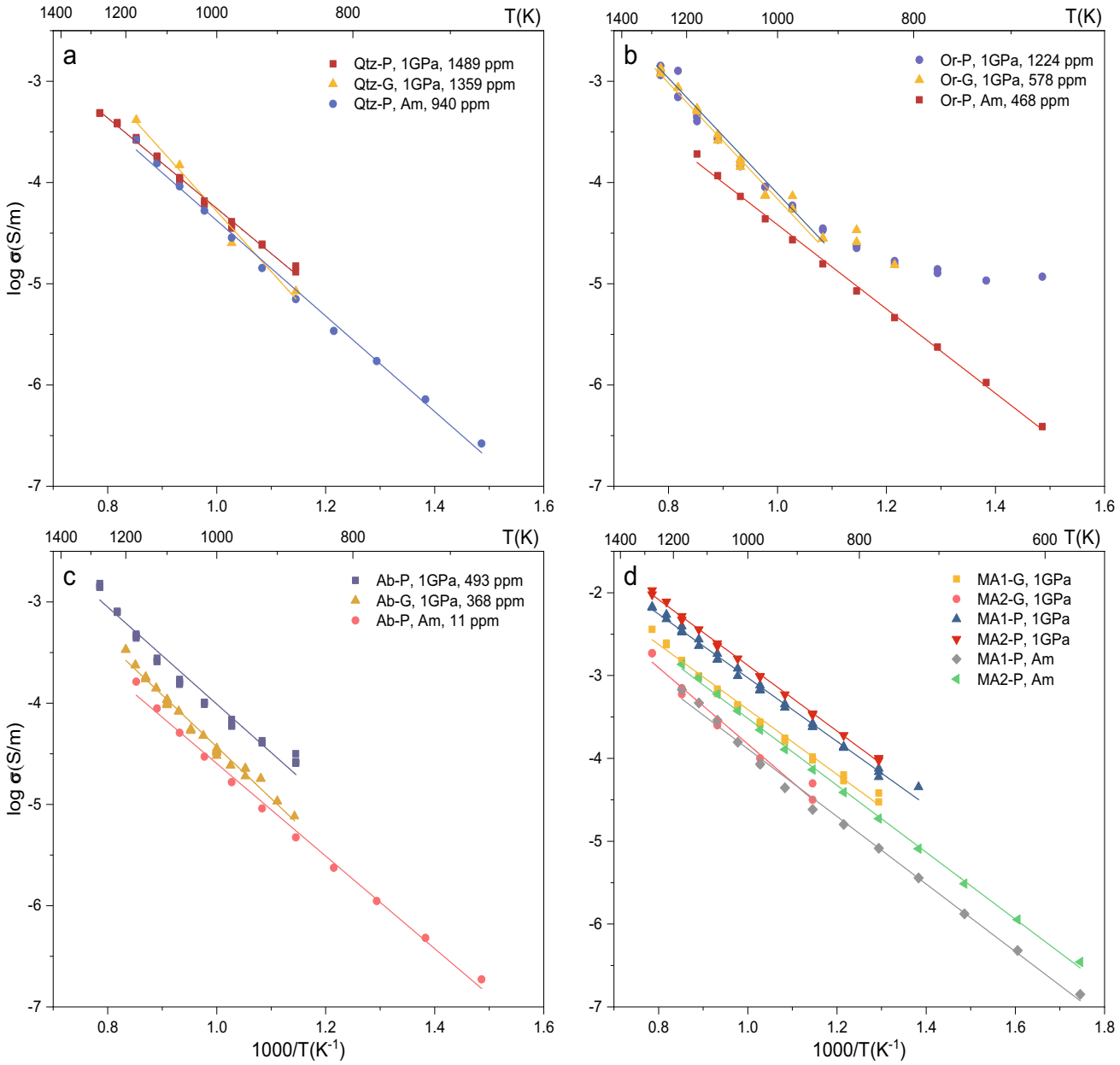

Fig. 4 Electrical conductivity vs. reciprocal temperature for single- and multiphase aggregates with different grain sizes at 1 GPa and ambient pressure. The single-phase aggregates include Qtz (**a**), Or (**b**) and Ab (**c**), and the multiphase aggregates include MA1 and MA2 (**d**). The data for each sample were derived from the cooling stage, except for Qtz-G at 1 GPa. For Or-P and Or-G at 1 GPa, only the conductivities above 923 K were fitted in **b**. The water contents of Qtz-P, Or-P, and Ab-P at ambient pressure were assumed to be same as those of their starting materials. The lines were fitted to the Arrhenius equation

the orthoclase in MA1-G, the elemental distributions of K^+, Na^+, and Si^{4+} were mapped using energy dispersive X-ray spectroscopy (EDS) (Fig. 7). This showed that K^+ had diffused from the orthoclase to the albite grains and Na^+ had diffused from the albite to the orthoclase grains, while Na^+ and K^+ had hardly diffused into the quartz grains. The zoning texture for both orthoclase and albite is ascribed to the diffusion of Na^+ and K^+ across grain boundaries. Compared to MA1-P in Fig. 6, the occurrence of diffusion was less pervasive in MA1-G. The concentration profiles illustrate the distances of about 40 μm that K^+ and Na^+ had diffused into the albite and orthoclase grains.

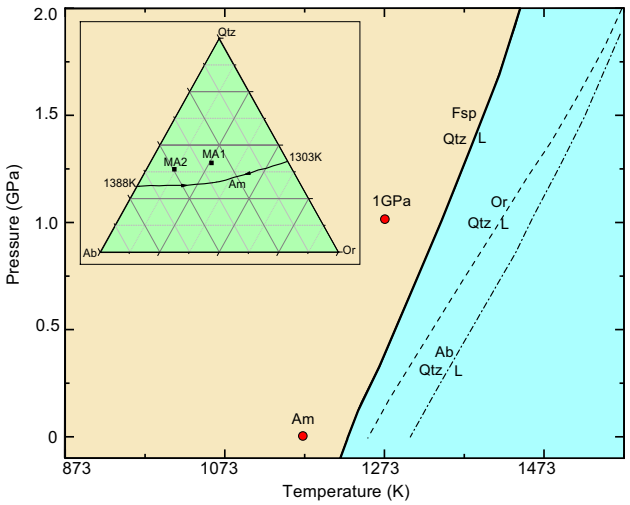

Fig. 5 Equilibrium melting diagram and pressure and temperature conditions for the measurements. The insert shows the quartz-feldspar cotectic in the Qtz-Ab-Or triangle (Tuttle and Bowen 1958). Also shown is the composition of the multiphase samples subjected to the conductivity measurements. The equilibrium diagram shows the approximate points of the solidus in the quartz-feldspar solid solution, and the Qtz-Ab and Qtz-Or melting systems (leucite is not shown as it forms only in more Or-rich compositions) (Huang and Wyllie 1975). Am, ambient pressure; Fsp-feldspar solid solution; Qtz, quartz; Or, orthoclase

Discussion

Water in the samples

At 1 GPa, the powder samples contained a few times more water than their starting materials, and the powder samples with smaller grain sizes had higher water contents, including Qtz and Ab (Fig. 2a, c). Such water was probably brought into the grain and powder aggregates during the hot-pressing process rather than during the electrical conductivity measurements, because the water content of Or-G without the hot-pressing treatment was similar to that of the starting material. During sample assembly for hot pressing, moisture might have been absorbed on the surface of the powdered minerals and more water will be incorporated into the grains at high pressure (Keppler and Rauch 2000). At ambient pressure, by contrast, little water can be incorporated into the samples due to the limited water solubility at this pressure. We believe that free water does not exist in the samples for the following reasons: (1) The activation enthalpy was relatively high (0.78–0.87 eV). In the case of free water existing at grain boundaries in polycrystalline brucite, the activation enthalpy is as low as 0.11 eV (Gasc et al. 2011); (2) If free water exists at grain boundaries, the bulk conductivity of the single-phase aggregates is expected to be much higher than those found in previous studies; however, this was not the case; (3) If free grain-boundary water overwhelms the grain-boundary ionic conduction proposed in this study, the measured bulk conductivity of the multiphase samples would be consistent with the model calibration based on the conductivity data of the single-phase aggregates containing water; (4) If free water exists, granitic samples will inevitably melt. However, no melts are found in the recovered samples. Consequently, we think that fractional water may have been stored at grain boundaries in the state of defect-related hydrogen rather than free water.

Conduction mechanisms

The bulk conductivity of single-phase aggregates is dominated by lattice conduction from the grain interior at both 1 GPa and ambient pressure. The electrical conductivities of Qtz-P and Or-P at 1 GPa were consistent with those of Qtz-G and Or-G, respectively, suggesting that conductivity is independent of grain size. When the grain size is less than a few microns, grain-boundary conduction could govern bulk conduction (Ten Grotenhuis et al. 2004), while it would be insignificant if the grain size is larger than dozens of microns (Yang and Heidelbach 2012). The average grain size of Ab-P, Or-P, and Qtz-P in our study was about 20 µm, and, consequently, their conductivity is attributed mainly to lattice conduction. Although the conductivity of quartz, orthoclase, and albite has been widely studied at both ambient pressure and 1 GPa, their conductivity and conduction mechanism may differ with their chemical compositions, which we will discuss individually below (Jain and Nowick 1982; Yang et al. 2012; Hu et al. 2013).

As shown in Fig. 8, the electrical conductivities of Qtz-P and Qtz-G at both 1 GPa and ambient pressure were comparable to those of polycrystalline quartz in previous studies (Bagdassarov and Delépine 2004). Due to the strong anisotropy of conductivity, the conductivities measured in our study were similar to that at an angle of 60° to the *Z*-axis (Fig. 8b) (Jain and Nowick 1982; Campone et al. 1995; Wang et al. 2010). Conduction in Qtz-P and Qtz-G could be attributed to the movement of H^+ in the crystals (Fig. 9a). The main conduction mechanism for quartz is generally believed to be ionic conduction resulting from the movement of charge carriers M^+ (e.g., Na^+, Li^+, or H^+) related to the Al-M centers (Campone et al. 1995; Jain and Nowick 1982). In our study, both Al^{3+} or Na^+ were absent from the quartz or were below the experimental detection limit (about 250 ppm) before and after the conductivity measurements. The charge carrier is, therefore, likely to have been the H^+ of hydroxyl (Aines and Rossman 1984). This is supported by the fact that Qtz-P has a similar activation enthalpy to quartz (0.98 eV), as reported by Jain and Nowick (1982), in which Na^+ is substituted by hydrogen. Qtz-P has a lower activation enthalpy at ambient pressure than Qtz-G at 1 GPa, probably

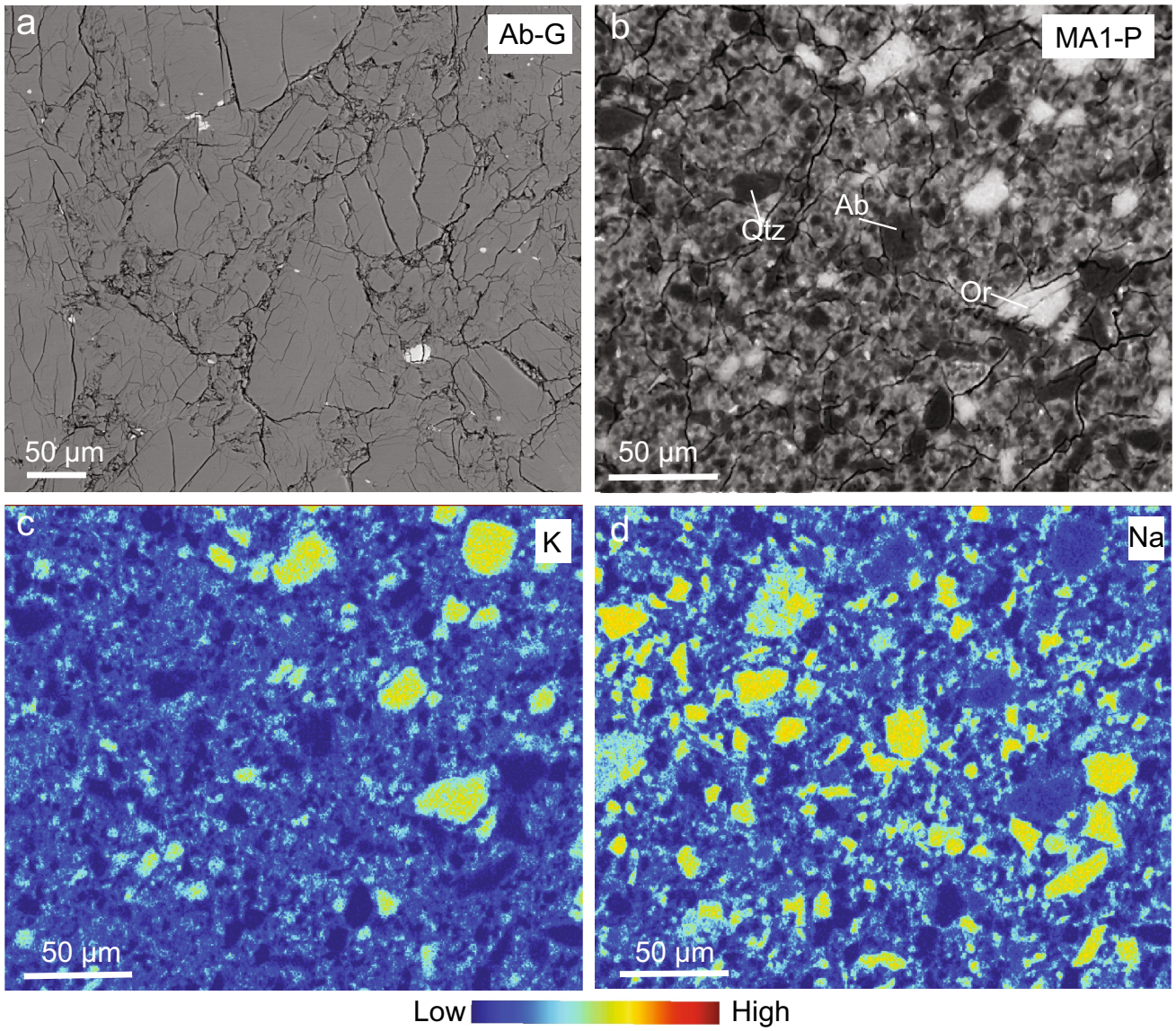

Fig. 6 Scanning electron microprobe images of: **a** Ab-G and **b** MA1-P at 1 GPa after the conductivity measurements; **c**, **d** denote the distribution of K^+ and Na^+ in MA1-P, respectively. No melts were found in either Ab-G or MA1-P. Albite grains of Ab-G had been crushed and microcracks had been generated within the grains. In MA1-P, microcracks were generated around the mineral grains

because the evaporation of the vinyl alcohol solution leaves the grain boundaries less compacted at ambient pressure.

The conductivity of orthoclase showed week anisotropy, and therefore, there were only slight differences between the conductivities found in this and previous studies (Maury 1968; Hu et al. 2013, 2014; Wang et al. 2014a) (Fig. 8). Conduction in orthoclase could be due to the hopping of K^+ in the lattice structure. The activation enthalpies of Or-P and Or-G at 1 GPa were similar to those of orthoclase (0.98 eV) and microcline (1.01 eV) reported by Hu et al. (2014) and Wang et al. (2014a), respectively. Since the albite lamellae in Or-R are not well connected, and even Na^+ diffusion occurs only within the orthoclase grains rather than throughout the whole grains of Or-G (Fig. S1), this rules out the possibility of Na^+ being the charge carrier in conduction. K^+ is, therefore, believed to have been the main charge carrier in the orthoclase examined in this study, diffusing among the vacancies in the crystal lattice (Fig. 9a) (Giletti and Shanahan 1997; Cherniak 2003).

For albite, alkali ions could be the main charge carriers. The conductivity of Ab-P at 1 GPa was similar to that of albite at ambient pressure and of plagioclase at 1.2 GPa (Maury 1968; Yang et al. 2012). However, the electrical conductivities of Ab-P and Ab-G at both pressures were lower than that of the other dry albite reported in previous studies (Guo et al. 2015; Hu et al. 2011, 2013), perhaps due to

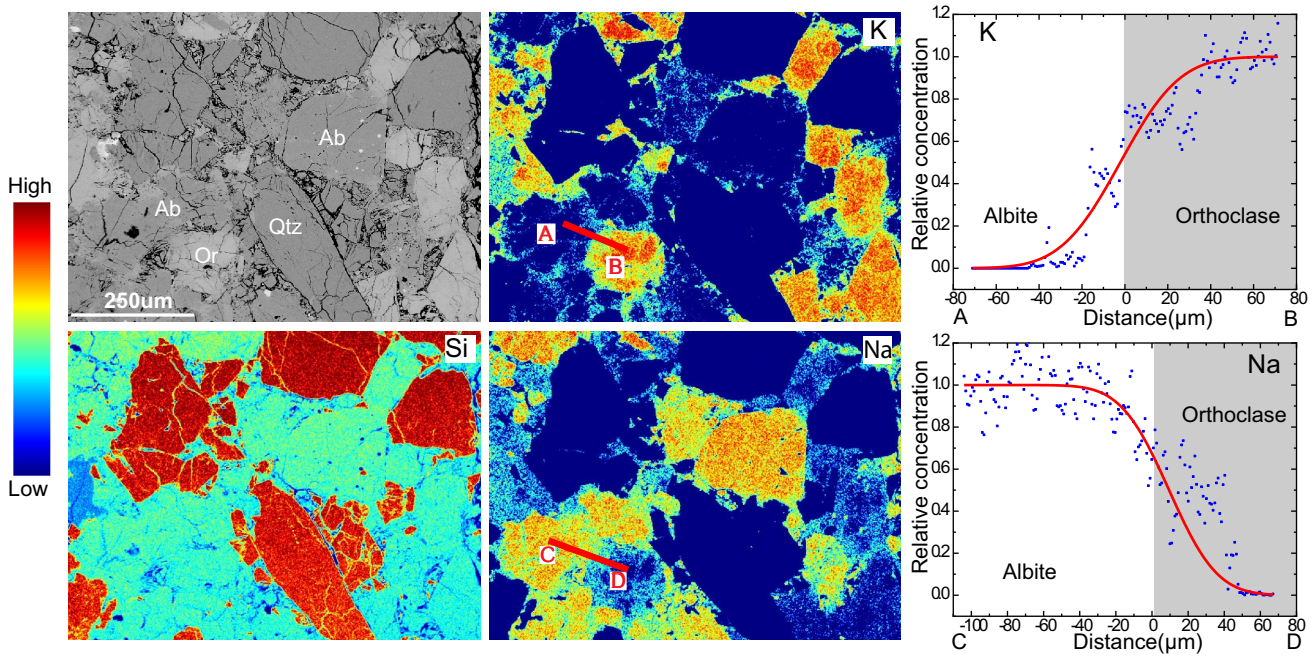

Fig. 7 Backscatter image of MA1-G after the electrical conductivity measurement (top left) and the energy dispersive X-ray spectroscopy (EDS) mapping images of K^+, Na^+, and Si^{4+} elements. The concentration vs. distance profiles of K^+ and Na^+ on the right correspond to the transverse lines, AB and CD. The concentrations of Na^+ and K^+ represent the relative values, while the values on the X-axis is the distance from the interface between the orthoclase and albite grains. The lines of best fit in the profiles are fitted using the diffusion couple model (Zhang and Cherniak 2010)

differences in composition. Candidates for the charge carriers in albite are H^+ and Na^+. Na^+ has been inferred to be the charge carrier not only in alkali feldspars but also in silicate melts and glasses because of its high diffusivity (Hu et al. 2011; Ni et al. 2011; Yang et al. 2012). Ab-G and Ab-P at both 1 GPa and ambient pressure have similar activation enthalpies to those found in previous studies, where Na^+ was supposed to be the main charge carrier (Hu et al. 2011). In addition, the concentration of K^+ is very low in Ab-R. Consequently, conduction in Ab-P and Ab-G could be due mainly to the movement of Na^+ in the interstices between the silicate tetrahedra (Giletti and Shanahan 1997; Hu et al. 2011). However, Yang et al. (2012) found that the electrical conductivity of plagioclases increases systematically with hydrogen and suggested that H^+, probably together with Na^+, acts as the charge carrier in "hydrous" plagioclase (Fig. 9a). Zhang et al. (2016) also suggested that conduction in hydrous feldspar may involve more than one mechanism based on calculations obtained with the cBΩ thermodynamic model. The relative contribution of H^+ and Na^+ to electrical conductivity is unknown and requires further study.

Electrical conductivity of multiphase aggregates

Figure 10a–c compares the electrical conductivities of single-phase and multiphase aggregates at 1 GPa and ambient pressure. At each pressure, both multiphase aggregates had appreciably higher conductivities than the three single-phase aggregates, regardless of grain sizes. To compare the measured conductivity of the multiphase aggregates with the calculated bulk conductivity, we used different mixing models to calculate the latter based on the electrical conductivity of each single-phase (Jones et al. 2012; Khan and Shankland 2012). The application of mixing models requires the constituents to satisfy the following assumptions: (1) the constituent minerals are in phase equilibrium, which means the absence of chemical exchange between the minerals; (2) grain-boundary conduction is negligible; and (3) the constituent minerals are randomly aligned and uniformly distributed (Hu et al. 2014; Yang et al. 2012). We combined the electrical conductivities of Ab-P, Or-P, and Qtz-P at ambient pressure to estimate the conductivity of MA1-P at ambient pressure using six different mixing models: geometric mean (GM), effective medium theory (EMT), Hashin–Shtrikman (HS) bound, Reuss (harmonic) mean, Voigt (arithmetic) mean, and the Voigt–Reuss–Hill model. Voigt and Reuss means, as well as HS, provide the lower and upper bounds (Hashin and Shtrikman 1961; Han and Clark 2021). Voigt–Reuss–Hill, GM, and EMT give estimates of the bulk electrical conductivity (Khan and Shankland 2012; Choy 2015). Although the mixing models produced a range of estimates for MA1-P, the measured conductivity of MA1-P

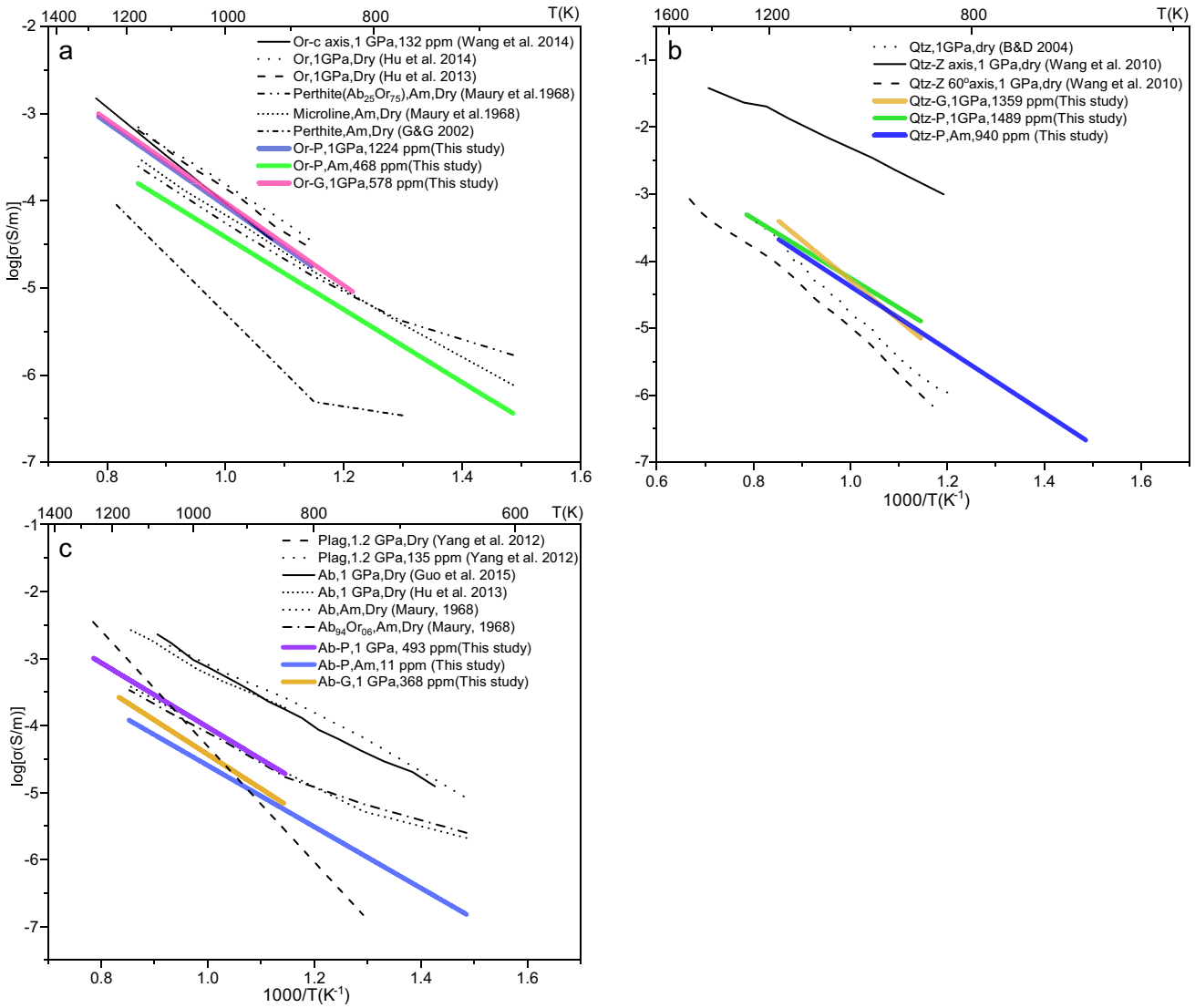

Fig. 8 Comparison of the electrical conductivities of: **a** orthoclase; **b** quartz, and **c** albite with previous studies

was more than half an order of magnitude higher than the maximum estimate according to the GM model (Fig. 10d). As the multiphase aggregates had much higher conductivities than the three single-phase aggregates at both 1 GPa and ambient pressure, the laboratory-measured conductivities of the multiphase aggregates were higher than all of the estimates from the mixing models.

The changes in conductivity during the measurements could provide key information explaining the discrepancies between the single-phase and multiphase aggregates. The electrical conductivities of MA1-G at 1 GPa were consistent with each other between the first heating–cooling cycle and the second heating stage below 1173 K (Fig. 11). It should be noted that the electrical conductivity of Or-G was consistent with that of MA1-G at heating stage 2 below 1173 K, implying that bulk conductivity was controlled by the interconnected orthoclase. However, the conductivity of MA1-G was about half an order of magnitude higher than that of Or-G as the temperature increased to 1273 K. This showed good reproducibility in the stages following heating stage 2, and the conductivity was more than half an order of magnitude higher than those measured before cooling stage 2. Analogous to MA1-G, bothMA1-P and the MA2-P at 1273 K and 1 GPa also showed an increase at the end of the first heating stage. This conductivity enhancement could be related to the grain boundary process resulting from Na–K interdiffusion between albite and the orthoclase grains initiated at a high temperature.

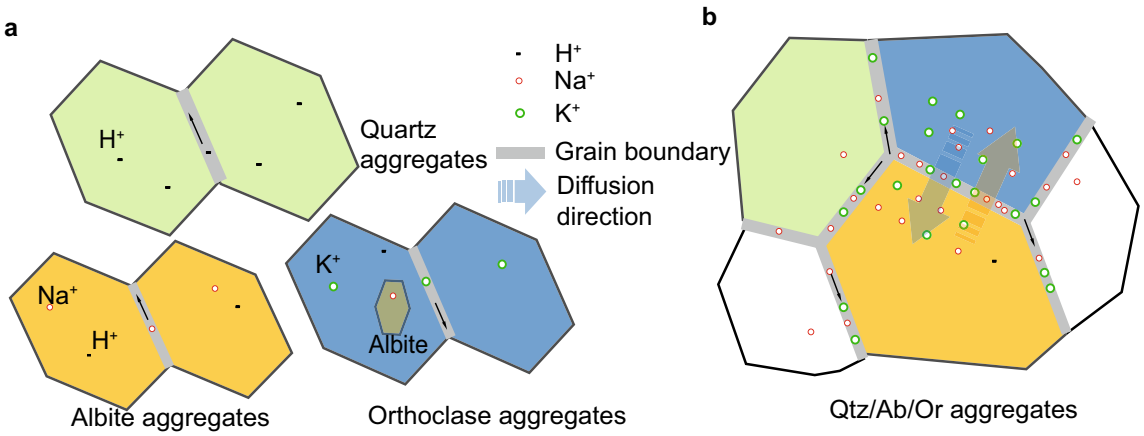

Fig. 9 Schematic diagram of the possible conduction mechanisms of: **a** single-phase aggregates and **b** the Qtz/Ab/Or multiphase aggregates. The black arrow denotes the movement of potential charge carriers at grain boundaries. The Na–K exchange between orthoclase and albite causes their migration and, hence, their lingering at grain boundaries

Grain-boundary ionic conduction

Interdiffusion of ions across albite-orthoclase grain boundaries is illustrated by the distribution of Na^+ and K^+ in MA1-G after the conductivity measurement (Fig. 7). The grain boundaries could be regarded as a separate phase or medium with a thickness of about 10 nm (Keller et al. 2007). In the interdiffusion process, some alkali ions have chances to diffuse into the grain boundary (GB) at a high temperature. For albite–orthoclase–quartz multiphase aggregates, the chemical gradient between orthoclase and albite will inevitably drive the diffusion process albite → GB → orthoclase for Na^+ and simultaneously orthoclase → GB → albite for K^+. This process is maintained until the equilibrium has been achieved. By contrast, the diffusion process is only albite → GB ← albite for Na^+ and orthoclase → GB ← orthoclase for K^+ in a single-phase aggregate, and this diffusion process will soon be suppressed due to the chemical equilibrium between adjacent grains and the short diffusion distance at grain boundaries. These Na^+ and K^+ ions can diffuse not only across the grain boundaries but also along them. As a result, more Na^+ and K^+ will be retained at the grain boundaries for multiphase samples, where interdiffusion occurs. Diffusion could be directly linked to electrical conductivity, σ, by the Nernst–Einstein relation:

$$\sigma = fDcq^2/kT \tag{3}$$

where f is a nondimensional constant indicating the geometrical factor, D is the diffusion coefficient of charge carriers, c is the concentration of these charge carriers, q is the electrical charge of the charge carriers, k is the Boltzmann constant, and T is the absolute temperature in K. Accordingly, compared to the single-phase aggregates, the higher concentration of alkali ions at grain boundaries in multiphase aggregates results in their higher electrical conductivities. In terms of activation enthalpy, our observation that multiphase aggregates had lower activation enthalpies than the constituent single-phase aggregates at both 1 GPa and ambient pressure (Table 2), implies that the migration of Na^+ and K^+ ions along grain boundaries is easier than in the crystal lattice. This is consistent with previous studies documented that the grain boundary diffusion have activation energy lower (about 1/3 less) than the lattice diffusion (Farver and Yund 1996). Therefore, we propose that the transport of alkali ions along grain boundaries (grain-boundary conduction) resulted in the higher electrical conductivities of the multiphase aggregates than their single-phase constituents and the overall conductivities modelled by these constituents.

Grain-boundary conduction due to the Na–K exchange between feldspars provides a novel mechanism for grain-boundary conduction, which is important for the multiphase systems. For grain-boundary conduction, previous studies have focuses mainly on either single-phase aggregates with varying grain sizes or aggregates containing a conductive phase, such as melts or graphite films (Roberts and Tyburczy 1991; Ducea and Park 2000; Ten Grotenhuis et al. 2004; Watson et al. 2010; Yang and Heidelbach 2012). Such conductive phases at grain boundaries were not considered as they were not observed in this study. In the studies mentioned above, grain-boundary conduction was related to the transport of defects. Grain-boundary conductivity dominates the bulk conductivity of aggregates for grain size smaller than 10 μm, above which this process is independent of grain size (Yang and Heidelbach 2012; Pommier et al. 2018). However, the conductivities of multiphase aggregates with grain sizes of 10–20 μm are approximately half an order of magnitude higher than those with grain sizes of 200 μm

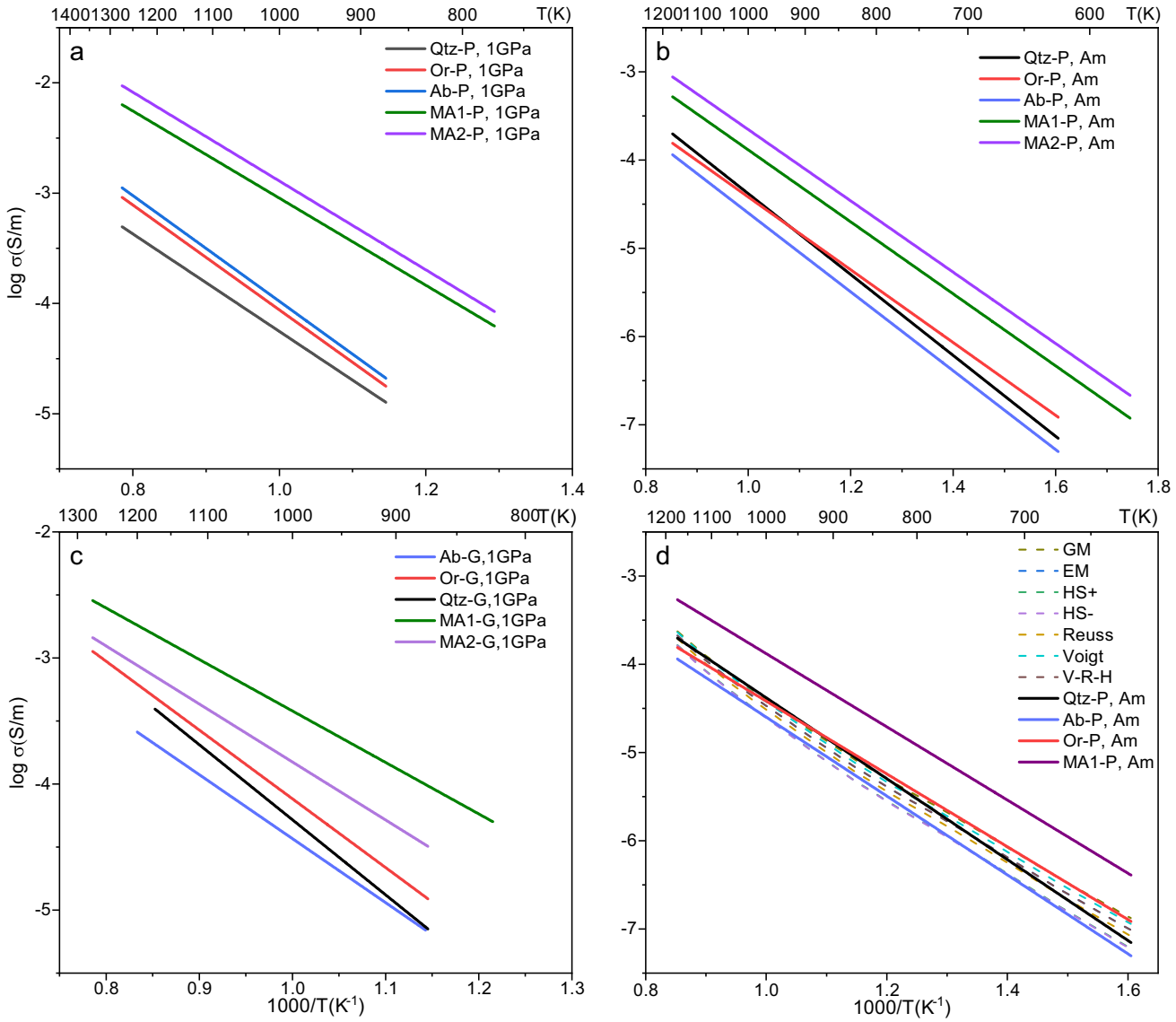

Fig. 10 Comparison of the electrical conductivities of the single-phase and multiphase aggregates with small grain sizes at: **a** 1 GPa and **b** ambient pressure; **c** comparison of the electrical conductivities of the single-phase and multiphase aggregates with large grain sizes at 1 GPa; **d** comparison of the electrical conductivity of MA1-P at ambient pressure with that calculated using various mixing models. The calculations shown by dashed lines were based on the modal composition of MA1-P. *GM* geometry mean, *EM* effective medium theory, HS^+ upper Hashin–Shtrikman bound, HS^- lower Hashin–Shtrikman bound, Reuss: harmonic mean; Voigt: arithmetic mean; V-R-H: Hill model (the average of Reuss and Voigt mean)

in this study (Fig. 10), indicating the dependence of grain-boundary conduction on grain size. Grain size affects the contribution of grain-boundary conductivity to bulk conductivity by controlling the volume fraction of grain boundaries in an aggregate (Waff 1974). Defect-related hydrogens at grain-boundary (not free water) may play an important role in explaining this discrepancy. Experimental studies have shown that if an H^+ flux exists at grain boundaries, grain-boundary diffusion might control the bulk diffusion of an aggregate despite a large grain size (Demouchy 2010), and this diffusion relationship has been used to calculate the grain-boundary and bulk conductivities of a peridotite (Jones 2016). Defect-related hydrogens could exert a positive influence in two ways: (1) dramatically increasing the diffusivity of alkali ions at grain boundaries (Costa and Chakraborty 2008); and (2) facilitating inter-diffusivity between adjacent feldspars and the segregation of alkali ions, which leads to a larger number of ions at grain boundaries (Zhang et al. 2019). As a result, in our study, the faster hydrogen-induced ionic migration along grain boundaries significantly enhanced the effect of grain-boundary conduction on the bulk conductivity, even for grain sizes as large as

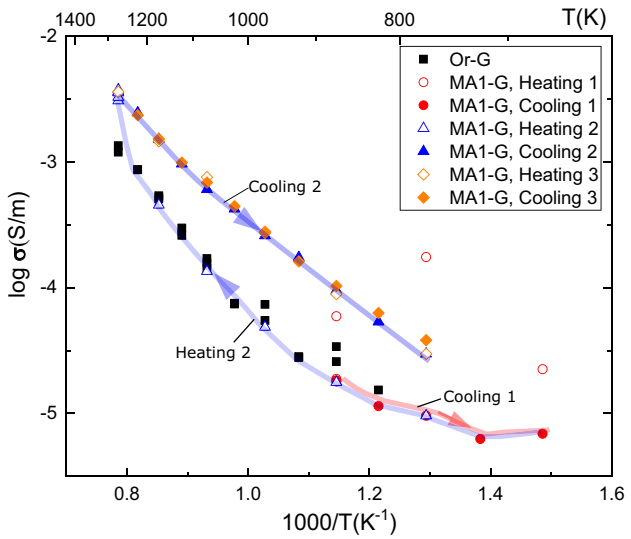

Fig. 11 Electrical conductivity of MA1-G and Or-G vs. reciprocal temperature at 1 GPa. The black solid square symbols represent the conductivities of Or-G during the different cooling stages. The transparent lines with arrows show the heating and cooling processes during the MA1-G conductivity measurement

200 µm. To our knowledge, this grain-boundary conduction by alkali ions has never been reported experimentally in a multiphase mineral aggregate. In addition, grain-boundary ionic conduction enhanced the bulk conductivity of powder multiphase aggregates at 1 GPa more than that at ambient pressure, probably indicating its dependence on pressure. This could be related to the generation of defects and strain by the high pressure at grain boundary regions, which facilitates the segregation of alkali ions to minimize strain energy and compensate for the space charge (Hiraga et al. 2004; Keller et al. 2007). However, we could not exclude the possibility that the interspaces among grains created by evaporating the vinyl alcohol binder solution might have hindered the alkali ions from being segregated and transported along grain boundaries at ambient pressure. Furthermore, the chemical compositions of the constituent minerals and their distribution might also affect grain-boundary ionic conduction by controlling the number of segregated ions at grain boundaries. A quantitative relationship between these factors that describes their enhancement is essential for determining the contribution of grain-boundary ionic conduction to bulk conductivity of rocks, and this will require further studies in the future.

This grain-boundary ionic conduction may account for the high electrical conductivity of the peridotite observed under the South Africa Craton. Jone (2016) proposed the grain-boundary conductivity associated with hydrogen to explain the observed higher conductivity than the values from mixing models, but it still requires a finer grain size or a much higher water content than the obtained xenoliths. As grain boundaries could be a reservoir for the incompatible elements, such as Al^{3+} and Ca^{2+}, the fast transport of these elements, facilitated by hydrogen, may contribute significantly to the bulk conductivity (Hiraga et al. 2004). Under the Tanlu fault, the observed lower conductivity as compared to the modelled values suggested that the grain boundary process is insignificant in the deep crust and/or the upper mantle. Instead, the chemical composition of rocks may differ from the xenolith on which the calculation of mixing models was based (Wang et al. 2014a, b, c). Therefore, in this scenario, it is important to accurately determine the chemical composition of the lithosphere when modelling the conductivity using mixing models.

Geological implication

MT observations have found that several high electrical conductivity anomalies are associated with shear zones (Selway 2018; DeLucia et al. 2019). (Wang et al. 2014c) observed that the Longmenshan Thrust Fault separating eastern Tibet and the Yangtze Craton extends to the middle-to-lower crust under Tibet in the eastern Tethyan domain, where a remarkably wide-spread layer with high conductivity (~0.1 S/m) and low velocity exists (Unsworth et al. 2004; Sol et al. 2007; Xu et al. 2007). This layer was suggested to be an integral decollement and shear zone due to the fact that the Songpan-Ganzi Block was expanding eastward and decoupled the upper crust from the middle crust (Bai et al. 2010; Wang et al. 2014c). For an active shear zone, relative motion generally involves mass transfer and grain-boundary diffusion during dynamic metamorphism (Goncalves et al. 2012). Since the crust of the Songpan-Ganzi Block is primarily granitoid and/or a felsic granulite phase and the influence of their modal composition on the bulk conductivity is limited, we used MA1 and MA2 to represent the middle crust of Tibet (Searle et al. 2011; Zi et al. 2013). The temperature of the middle crust (30–40 km) was assumed to be approximately 1073 K based on the high surface heat flow at Songpan-Ganzi, which could be 80–110 mW/m^2 (Xu et al. 2011). We modeled the bulk conductivity of MA1 and MA2 below 20 µm and compared it with the observed electrical conductivity of the middle-to-lower crust of the Songpan-Ganzi Block (Fig. 12). The bulk conductivity comprised the grain-interior and grain-boundary conductivities (Eq. 4) developed by Ten Grotenhuis et al. (2004). To quantify the grain-boundary ionic conductivity, we used the measured conductivity of MA1 and MA2 at 1073 K and 1 GPa, and fitted the data to the relationship between grain size and bulk conductivity. The conductivity of the grain interior was calculated from the conductivity of Ab-P, Or-P, and Qtz-P at 1 GPa using EMT, which gives a decent average conductivity for a mixture (Han and Clark 2021) (Eq. 5):

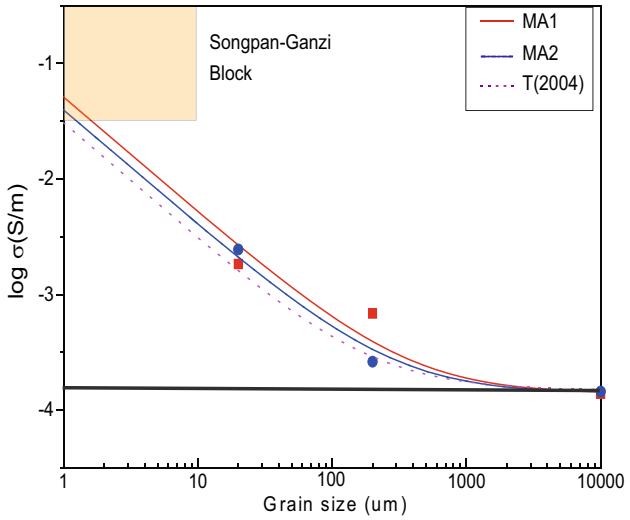

Fig. 12 Dependence of bulk electrical conductivity on grain size. The solid black line denotes the bulk conductivity of the grain interior calculated from the Eq. (4). The purple dotted line denotes the bulk conductivity adapted from the model of Ten Grotenhuis et al. (2004). MA1 (red solid line) and MA2 (blue solid line) are the best fitting curves based on MA1-G and MA1-P (red solid line), MA2-G, and MA2-P (blue dots), respectively, at 1 GPa and 1073 K. The grain size of MA1-G and MA2-G was set at 200 μm, while that of MA1-P and MA1-P was set at 20 μm. The orange shaded area denotes the conductivity of the middle crust under the Songpan-Ganzi block, in Tibet (Wang et al. 2014c)

$$\sigma_t = \sigma_{gi} + \sigma_{gb}\left(1 - (1 - 3\delta/d)^{2/3}\right) \quad (4)$$

$$\sum f_i\left(\frac{\sigma_i - \sigma_{\mathrm{gi}}}{\sigma_i + 2\sigma_{\mathrm{gi}}}\right) = 0 \quad (5)$$

where σ_{gi} is the bulk conductivity of the grain interior, σ_{gb} is the grain-boundary ionic conductivity, δ is the width of a grain boundary (here we take 1 nm (Demouchy 2010)), d is the grain size, and σ_i and f_i are the conductivity and volume percentage of the ith phase, respectively. MA1 and MA2 showed similar grain-interior conductivities due to the small differences among Ab-P, Or-P, and Qtz-P (Fig. 12). The resultant grain-boundary conductivities of MA1 and MA2 were 17.4 ± 2.6 and 23.0 ± 0.8 S/m, respectively. Such grain-boundary conductivities are five orders of magnitude greater than the grain-interior conductivity, consistent with grain-boundary diffusivity compared to grain-interior diffusivity (Farver and Yund 1996). When the grain size is relatively small (i.e., < 100 μm), the bulk conductivity is dominated by grain-boundary conductivity. As the grain size increases to approximately 1000 μm, the bulk conductivity is attributable mainly to the grain-interior conductivity due to the negligible grain-boundary conductivity.

To account for the bulk conductivity of 0.1 S/m at the middle crust of the Songpan-Ganzi Block in Tibet, a fine grain size (approximately 1–2 μm) was required in the active shear zone. The fault gouge revealed that the grain size of mylonites can be a few microns in the Longmenshan Fault (Li et al. 2015). Therefore, if the shear zone with such a fine grain size can extend to the middle-to-lower crust, the highly conductive anomaly could be attributed to the fast transport of alkalis ions along grain boundaries. Furthermore, as we only considered the major minerals of granitic rock, the influence of the minor minerals could also be important, but it was neglected in our study. Given the high temperature under the Songpan-Ganzi Block, the dehydration melting of amphibole and mica could enhance the bulk conductivity, as the perspective of crustal flow has suggested (Unsworth et al. 2004; Bai et al. 2010; Aranovich et al. 2014). In addition, seismic observations suggest a weak middle-to-lower crust that is characterised by low-viscosity and low velocity, allowing the Songpan-Ganzi upper crust to thrust eastwards (Zhang et al. 2009). However, several xenoliths suggested a dry middle-to-lower crust under Tibet (Hacker et al. 2000). Therefore, whether the fluid/melt phase is present in this region is still under debate. Our study provides a new insight into the origin of this high conductivity anomaly. We believe the reduction of the grain size in the shear zone will significantly increase the grain boundary conductivity as illustrated by this study. This new model is competitive to the fluid model and the partial melting model although it cannot rule out the other models (Ducea and Park 2000; Wang et al. 2013; Guo et al. 2015).

Supplementary Information The online version contains supplementary material available at https://doi.org/10.1007/s00410-021-01841-1.

Acknowledgements We would like to sincerely thank Dr. Xiong Wang, Jiayuan Bai, Prof. Christopher Ling and Dr. Qingbo, Xia for the help in conducting experiments, as well as the input from Dr Richard Flood. We are grateful to Prof. Martyn Unsworth for the constructive suggestions. This work is supported by the Natural Science Foundation of China (91755215, 42072051), CAS "Light of West China" program (Y9CR026 to X. G.), Australian Research Council Discovery Project DP160103502 and Open Research Program GPMR201801 funded by State Key Laboratory of Geological Processes and Mineral Resources, China University of Geosciences, Wuhan. Kui Han would like to thank Macquarie University for an International Research Training Scholarship (iRTP) and Chengdu University of Technology for starting-up grant (10912-KYQD2020-08600) and (80000-2020ZF11409). This work is indebted to the Australian Research Council (ARC) Centre of Excellence for Core to Crust Fluid System for facilitating the research work. All of the data reported in this paper is available through EarthChem Library (https://doi.org/10.26022/IEDA/111815).

References

Adam J, Green TH (1994) The effects of pressure and temperature on the partitioning of Ti, Sr and REE between amphibole, clinopyroxene and basanitic melts. Chem Geol 117:219–233

Aines RD, Rossman GR (1984) Water in minerals? A peak in the infrared. J Geophys Res Solid Earth 89:4059–4071

Amulele GM, Lanati AW, Clark SM (2019) Electrical conductivity studies on silica phases and the effects of phase transformation. Ame Miner 104:1800–1805. https://doi.org/10.2138/am-2019-7120

Aranovich LY, Makhluf AR, Manning CE, Newton RC (2014) Dehydration melting and the relationship between granites and granulites. Precambrian Res 253:26–37

Aubaud C, Hauri EH, Hirschmann MM (2004) Hydrogen partition coefficients between nominally anhydrous minerals and basaltic melts. Geophys Res Lett 31:1–4. https://doi.org/10.1029/2004GL021341

Bagdassarov NS, Delépine N (2004) α–β inversion in quartz from low frequency electrical impedance spectroscopy. J Phys Chem Solids 65:1517–1526

Bai D, Unsworth MJ, Meju MA, Ma X, Teng J, Kong X, Sun Y, Sun J, Wang L, Jiang C, Zhao C, Xiao P, Liu M (2010) Crustal deformation of the eastern Tibetan plateau revealed by magnetotelluric imaging. Nature Geosci 3:358–362. https://doi.org/10.1038/ngeo830

Campone P, Magliocco M, Spinolo G, Vedda A (1995) Ionic transport in crystalline SiO2: THE role of alkali-metal ions and hydrogen impurities. Phys Rev B 52:15903–15908. https://doi.org/10.1103/PhysRevB.52.15903

Cherniak DJ (2003) REE diffusion in feldspar. Chem Geol 193:25–41. https://doi.org/10.1016/S0009-2541(02)00246-2

Choy TC (2015) Effective medium theory: principles and applications. Oxford University Press, Oxford

Costa F, Chakraborty S (2008) The effect of water on Si and O diffusion rates in olivine and implications for transport properties and processes in the upper mantle. Phys Earth Planet Inter 166:11–29. https://doi.org/10.1016/j.pepi.2007.10.006

Dai L, Karato S (2020) Electrical conductivity of Ti-bearing hydrous olivine aggregates at high temperature and high pressure. Solid Earth, J Geophys Res. https://doi.org/10.1029/2020JB020309

DeLucia MS, Murphy BS, Marshak S, Egbert GD (2019) The Missouri high-conductivity belt, revealed by magnetotelluric imaging: evidence of a trans-lithospheric shear zone beneath the Ozark Plateau, Midcontinent USA? Tectonophys 753:111–123. https://doi.org/10.1016/j.tecto.2019.01.011

Demouchy S (2010) Diffusion of hydrogen in olivine grain boundaries and implications for the survival of water-rich zones in the Earth's mantle. Earth Planet Sci Lett 295:305–313

Dohmen R (2008) A new experimental thin film approach to study mobility and partitioning of elements in grain boundaries: Fe-Mg exchange between olivines mediated by transport through an inert grain boundary. Am Miner 93:863–874. https://doi.org/10.2138/am.2008.2671

Dohmen R, Milke R (2010) Diffusion in polycrystalline materials: grain boundaries, mathematical models, and experimental data. Rev Miner Geochem 72:921–970. https://doi.org/10.2138/rmg.2010.72.21

Ducea MN, Park SK (2000) Enhanced mantle conductivity from sulfide minerals, southern Sierra Nevada, California. Geophys Res Lett 27:2405–2408. https://doi.org/10.1029/2000GL011565

Farver JR, Yund RA (1996) Volume and grain boundary diffusion of calcium in natural and hot-pressed calcite aggregates. Contrib Mineral Petrol 123:77–91. https://doi.org/10.1007/s004100050144

Farver JR, Yund RA, Rubie DC (1994) Magnesium grain boundary diffusion in forsterite aggregates at 1000°–1300°C and 0.1 MPa to 10 GPa. J Geophys Res Solid Earth 99:19809–19819. https://doi.org/10.1029/94JB01250

Fei H, Druzhbin D, Katsura T (2020) The effect of water on ionic conductivity in olivine. J Geophys Res Solid Earth. https://doi.org/10.1029/2019JB019313

Gasc J, Brunet F, Bagdassarov N, Morales-Flórez V (2011) Electrical conductivity of polycrystalline $Mg(OH)_2$ at 2 GPa: effect of grain boundary hydration–dehydration. Phys Chem Minerals 38:543–556. https://doi.org/10.1007/s00269-011-0426-3

Giletti BJ, Shanahan TM (1997) Alkali diffusion in plagioclase feldspar. Chem Geol 139:3–20. https://doi.org/10.1016/S0009-2541(97)00026-0

Goncalves P, Oliot E, Marquer D, Connolly J (2012) Role of chemical processes on shear zone formation: an example from the Grimsel metagranodiorite (Aar massif, Central Alps). J Metamorph Geol 30:1–20. https://doi.org/10.1111/j.1525-1314.2012.00991.x

Grant K, Ingrin J, Lorand JP, Dumas P (2007) Water partitioning between mantle minerals from peridotite xenoliths. Contrib Mineral Petrol 154:15–34. https://doi.org/10.1007/s00410-006-0177-1

Guo X, Yoshino T, Shimojuku A (2015) Electrical conductivity of albite-(quartz)-water and albite-water-NaCl systems and its implication to the high conductivity anomalies in the continental crust. Earth Planet Sci Lett 412:1–9

Guo X, Zhang L, Su X, Mao Z, Gao X-Y, Yang X, Ni H (2018) Melting inside the tibetan crust? Constraint from electrical conductivity of peraluminous granitic melt. Geophys Res Lett 45:3906–3913. https://doi.org/10.1029/2018GL077804

Hacker BR, Gnos E, Ratschbacher L, Grove M, McWilliams M, Sobolev S, Wan J, Wu Z (2000) Hot and dry deep crustal xenoliths from tibet. Science 287:2463–2466. https://doi.org/10.1126/science.287.5462.2463

Han K, Clark SM (2021) Review of calculating the electrical conductivity of mineral aggregates from constituent conductivities. Solid Earth Sci 6:111–128. https://doi.org/10.1016/j.sesci.2021.02.003

Hashin Z, Shtrikman S (1961) Note on a variational approach to the theory of composite elastic materials. J Franklin Inst 271:336–341

Hiraga T, Anderson IM, Kohlstedt DL (2004) Grain boundaries as reservoirs of incompatible elements in the Earth's mantle. Nature 427:699. https://doi.org/10.1038/nature02259

Hu H, Li H, Dai L, Shan S, Zhu C (2011) Electrical conductivity of albite at high temperatures and high pressures. Am Miner 96:1821–1827

Hu H, Li H, Dai L, Shan S, Zhu C (2013) Electrical conductivity of alkali feldspar solid solutions at high temperatures and high pressures. Phys Chem Miner 40:51–62

Hu H, Dai L, Li H, Jiang J, Hui K (2014) Electrical conductivity of K-feldspar at high temperature and high pressure. Mineral Petrol 108:609–618

Huang W-L, Wyllie PJ (1975) Melting reactions in the system $NaAlSi_3O_8$-$KAlSi_3O_8$-SiO_2 to 35 kilobars, dry and with excess water. J Geol 83:737–748. https://doi.org/10.1086/628165

Jain H, Nowick AS (1982) Electrical conductivity of synthetic and natural quartz crystals. J Appl Phys 53:477–484

Johannes W, Holtz F (2012) Petrogenesis and experimental petrology of granitic rocks. Springer Science & Business Media, Berlin, pp 35–38

Johnson EA, Rossman GR (2004) A survey of hydrous species and concentrations in igneous feldspars. Am Miner 89:586–600. https://doi.org/10.2138/am-2004-0413

Jones AG (2016) Proton conduction and hydrogen diffusion in olivine: an attempt to reconcile laboratory and field observations and implications for the role of grain boundary diffusion in enhancing conductivity. Phys Chem Miner 43:237–265

Jones AG, Fullea J, Evans RL, Muller MR (2012) Water in cratonic lithosphere: calibrating laboratory-determined models of electrical conductivity of mantle minerals using geophysical and petrological observations. Geochem Geophys Geosyst 13:1–27

Karato S (2019) Some remarks on hydrogen-assisted electrical conductivity in olivine and other minerals. Prog Earth Planet Sci 6:55. https://doi.org/10.1186/s40645-019-0301-2

Karato S, Wang D (2013) Electrical conductivity of minerals and rocks. Physics and chemistry of the deep earth, 1st edn. John Wiley & Sons, Hoboken, pp 145–182

Keller LM, Hauzenberger CA, Abart R (2007) Diffusion along interphase boundaries and its effect on retrograde zoning patterns of metamorphic minerals. Contrib Mineral Petrol 154:205–216. https://doi.org/10.1007/s00410-007-0188-6

Keppler H, Rauch M (2000) Water solubility in nominally anhydrous minerals measured by FTIR and 1H MAS NMR: the effect of sample preparation. Phys Chem Miner 27:371–376. https://doi.org/10.1007/s002699900070

Khan A, Shankland TJ (2012) A geophysical perspective on mantle water content and melting: Inverting electromagnetic sounding data using laboratory-based electrical conductivity profiles. Earth Planet Sci Lett 317:27–43

Laumonier M, Farla R, Frost DJ, Katsura T, Marquardt K, Bouvier A-S, Baumgartner LP (2017) Experimental determination of melt interconnectivity and electrical conductivity in the upper mantle. Earth Planet Sci Lett 463:286–297

Li H, Xue L, Brodsky EE, Mori JJ, Fulton PM, Wang H, Kano Y, Yun K, Harris RN, Gong Z, Li C, Si J, Sun Z, Pei J, Zheng Y, Xu Z (2015) Long-term temperature records following the Mw7.9 Wenchuan (China) earthquake are consistent with low friction. Geol 43:163–166. https://doi.org/10.1130/G35515.1

Li Y, Jiang H, Yang X (2017) Fluorine follows water: Effect on electrical conductivity of silicate minerals by experimental constraints from phlogopite. Geochim Cosmochim Acta 217:16–27. https://doi.org/10.1016/j.gca.2017.08.020

Li P, Guo X, Chen S, Wang C, Yang J, Zhou X (2018) Electrical conductivity of the plagioclase–NaCl–water system and its implication for the high conductivity anomalies in the mid-lower crust of Tibet Plateau. Contrib Mineral Petrol 173:16. https://doi.org/10.1007/s00410-018-1442-9

Maury R (1968) Conductibilite electrique des tectosilicates. I. Methode Et Resultats Experimentaux Bull Minér 91:267–278

Mosenfelder JL, Rossman GR, Johnson EA (2015) Hydrous species in feldspars: a reassessment based on FTIR and SIMS. Am Miner 100:1209–1221

Ni H, Keppler H, Manthilake M, Katsura T (2011) Electrical conductivity of dry and hydrous NaAlSi 3 O 8 glasses and liquids at high pressures. Contrib Mineral Petrol 162:501–513

Nover G (2005) Electrical properties of crustal and mantle rocks–a review of laboratory measurements and their explanation. Surv Geophys 26:593–651

Özaydın S, Selway K (2020) MATE: an analysis tool for the interpretation of magnetotelluric models of the mantle. Geochem Geophys Geosyst. https://doi.org/10.1029/2020GC009126

Poe BT, Romano C, Nestola F, Smyth JR (2010) Electrical conductivity anisotropy of dry and hydrous olivine at 8 GPa. Phys Earth Planet Inter 181:103–111

Pommier A, Kohlstedt DL, Hansen LN, Mackwell S, Tasaka M, Heidelbach F, Leinenweber K (2018) Transport properties of olivine grain boundaries from electrical conductivity experiments. Contrib Mineral Petrol 173:41. https://doi.org/10.1007/s00410-018-1468-z

Roberts JJ, Tyburczy JA (1991) Frequency dependent electrical properties of polycrystalline olivine compacts. J Geophys Res Solid Earth 96:16205–16222

Robertson K, Heinson G, Thiel S (2016) Lithospheric reworking at the Proterozoic–Phanerozoic transition of Australia imaged using AusLAMP Magnetotelluric data. Earth Planet Sci Lett 452:27–35. https://doi.org/10.1016/j.epsl.2016.07.036

Rossman GR (2006) Analytical methods for measuring water in nominally anhydrous minerals. Rev Miner Geochem 62:1–28. https://doi.org/10.2138/rmg.2006.62.1

Searle MP, Elliott JR, Phillips RJ, Chung S-L (2011) Crustal–lithospheric structure and continental extrusion of Tibet. J Geol Soc 168:633–672

Selway K (2018) Electrical discontinuities in the continental lithosphere imaged with magnetotellurics. In: Lithospheric discontinuities. Am Geophys Union (AGU), pp 89–109

Sol S, Meltzer A, Bürgmann R, van der Hilst RD, King R, Chen Z, Koons PO, Lev E, Liu YP, Zeitler PK, Zhang X, Zhang J, Zurek B (2007) Geodynamics of the southeastern Tibetan Plateau from seismic anisotropy and geodesy. Geology 35:563–566. https://doi.org/10.1130/G23408A.1

Ten Grotenhuis SM, Drury MR, Peach CJ, Spiers CJ (2004) Electrical properties of fine-grained olivine: evidence for grain boundary transport. J Geophys Res Solid Earth 109:1–9

Thomas SM, Koch-Müller M, Reichart P, Rhede D, Thomas R, Wirth R, Matsyuk S (2009) IR calibrations for water determination in olivine, r-GeO_2, and SiO_2 polymorphs. Phys Chem Miner 36:489–509

Tuttle OF, Bowen NL (1958) Origin of granite in the light of experimental studies in the system $NaAlSi_3O_8$–$KAlSi_3O_8$–SiO_2–H_2O. In: Geological society of America memoirs. Geol Soc Am, pp 1–146

Unsworth M, Wenbo W, Jones AG, Li S, Bedrosian P, Booker J, Sheng J, Ming D, Handong T (2004) Crustal and upper mantle structure of northern Tibet imaged with magnetotelluric data. J Geophys Res Solid Earth 109:B02403. https://doi.org/10.1029/2002JB002305

Waff HS (1974) Theoretical considerations of electrical conductivity in a partially molten mantle and implications for geothermometry. J Geophys Res 79:4003–4010

Wang D, Li H, Yi L, Matsuzaki T, Yoshino T (2010) Anisotropy of synthetic quartz electrical conductivity at high pressure and temperature. J Geophys Res Solid Earth 115:1–10

Wang D, Karato S, Jiang Z (2013) An experimental study of the influence of graphite on the electrical conductivity of olivine aggregates. Geophys Res Lett 40:2028–2032. https://doi.org/10.1002/grl.50471

Wang D, Yu Y, Zhou Y (2014a) Electrical conductivity anisotropy in alkali feldspar at high temperature and pressure. High Pressure Res 34:297–308

Wang Q, Bagdassarov N, Xia Q-K, Zhu B (2014b) Water contents and electrical conductivity of peridotite xenoliths from the North China Craton: implications for water distribution in the upper mantle. Lithos 189:105–126. https://doi.org/10.1016/j.lithos.2013.08.005

Wang X, Zhang G, Fang H, Luo W, Zhang W, Zhong Q, Cai X, Luo H (2014c) Crust and upper mantle resistivity structure at middle section of Longmenshan, eastern Tibetan plateau. Tectonophysics 619:143–148. https://doi.org/10.1016/j.tecto.2013.09.011

Watson HC, Roberts JJ, Tyburczy JA (2010) Effect of conductive impurities on electrical conductivity in polycrystalline olivine. Geophys Res Lett 37:1–6. https://doi.org/10.1029/2009GL041566

Xu L, Rondenay S, van der Hilst RD (2007) Structure of the crust beneath the southeastern Tibetan Plateau from teleseismic receiver functions. Phys Earth Planet Inter 165:176–193. https://doi.org/10.1016/j.pepi.2007.09.002

Xu M, Zhu C, Rao S, Hu S (2011) Difference of thermal structure between eastern edge of Tibet Plateau and weasten Sichuan Basin. Sci Geol Sin 46:203–212

Yang X, Heidelbach F (2012) Grain size effect on the electrical conductivity of clinopyroxene. Contrib Mineral Petrol 163:939–947

Yang X, Keppler H, McCammon C, Ni H (2012) Electrical conductivity of orthopyroxene and plagioclase in the lower crust. Contrib Mineral Petrol 163:33–48

Yoshino T, Noritake F (2011) Unstable graphite films on grain boundaries in crustal rocks. Earth Planet Sci Lett 306:186–192. https://doi.org/10.1016/j.epsl.2011.04.003

Yoshino T, Matsuzaki T, Shatskiy A, Katsura T (2009) The effect of water on the electrical conductivity of olivine aggregates and its implications for the electrical structure of the upper mantle. Earth Planet Sci Lett 288:291–300

Zhang Y, Cherniak DJ (2010) Diffusion in minerals and melts: introduction. Rev Miner Geochem 72:1–4. https://doi.org/10.2138/rmg.2010.72.1

Zhang Z, Wang Y, Chen Y, Bai Z, Tian X, Li Q (2009) Crustal structure across Longmenshan fault belt from passive source seismic profiling. Geophys Res Lett 36:L17310. https://doi.org/10.1029/2009GL039580

Zhang B, Shan S, Wu X (2016) Modeling H, Na, and K diffusion in plagioclase feldspar by relating point defect parameters to bulk properties. Phys Chem Miner 43:151–159. https://doi.org/10.1007/s00269-015-0782-5

Zhang B, Li B, Zhao C, Yang X (2019) Large effect of water on Fe–Mg interdiffusion in garnet. Earth Planet Sci Lett 505:20–29. https://doi.org/10.1016/j.epsl.2018.10.015

Zi J-W, Cawood PA, Fan W-M, Eric T, Wang Y-J, McCuaig TC, Peng T-P (2013) Late permian-triassic magmatic evolution in the jinshajiang orogenic belt, Sw China and implications for orogenic processes following closure of the paleo-tethys. Am J Sci 313:81–112. https://doi.org/10.2475/02.2013.02